Theoretical and Applied Mechanics Letters 15 (2025) 100618

Contents lists available at ScienceDirect

Theoretical and Applied Mechanics Letters

journal homepage: www.elsevier.com/locate/taml

Research Article

Computational method for analytical solution with finite elements (CMAS-FE): Deriving approximate analytical solution for an isotropic homogeneous elastic medium with linear finite element method

Jiajia Yue[a], Zifeng Yuan[a,b,c,*]

[a] HEDPS, Center for Applied Physics and Technology, School of Mechanics and Engineering Science, Peking University, Beijing 100871, China
[b] State Key Laboratory for Turbulence and Complex Systems, Peking University, Beijing 100871, China
[c] Peking University Nanchang Innovation Institute, Nanchang 330000, China

ARTICLE INFO

Keywords:
CMAS-FE
Finite element method
Linear elastic problem
Analytical solution

ABSTRACT

This study presents a novel methodology to obtain an approximate analytical solution for an isotropic homogeneous elastic medium with displacement and traction boundary conditions. The solution is derived through solving a specific numerical problem under the scope of the linear finite element method (LFEM), so the method is termed computational method for analytical solutions with finite elements (CMAS-FE). The primary objective of the CMAS-FE is to construct analytical expressions for displacements and reaction forces at nodes, as well as for strains and stresses at elemental quadrature points, all of which are formulated as infinite series solutions of various orders of Poisson's ratios. Like the conventional LFEM, the CMAS-FE forms global sparse linear equations, but the Young's modulus and Poisson's ratio remain variables (or symbols). By employing a direct inverse method to solve these symbolic linear systems, an analytical expression of the displacement field can be constructed. The CMAS-FE is validated via patch and bending tests, which demonstrate convergence with mesh and term refinement. Furthermore, the CMAS-FE is applied to obtain the bending stiffness of a beam structure and to estimate an approximate stress intensity factor for a straight crack within a square-shaped plate.

1. Introduction

Linear elastic problems play an important role in the history of solid mechanics. The equilibrium equation, the geometry equation, and the general Hooke's law form the governing equations. One may then obtain various mechanical fields by solving the governing equations over one domain with proper displacement and traction boundary conditions. When the geometry of the domain is simple, we may obtain analytical solutions. Compared with numerical approaches, the computational cost of the evaluation of the mechanical quantity through the analytical solution is negligible. Moreover, analytical solutions play a vital role as benchmarks for validating numerical methods, providing a deeper comprehension of the underlying mechanical principles.

However, it may not be easy to find an analytical solution even for the linear elastic problem over one arbitrary domain. To overcome the inherent constraints of analytical solutions, various numerical methods have been developed. One of the most widely used numerical methods is the finite element method (FEM) because of its versatility in complex geometries and nonlinearities. The FEM discretizes the domain into finite elements and approximates the mechanical field with a proper interpolation scheme, which may have a significant computational cost depending on the number of degrees-of-freedom. The FEM struggles with computational efficiencies near singularities (e.g., crack tips) and may require remeshing for evolving discontinuities. Until now, seeking analytical solution is still important in theoretical and computational solid mechanics. Lü et al. [1] derived semi-analytical 3D elasticity solutions for orthotropic multi-directional functionally graded plates. Korelc [2] proposed finite element solution in terms of selected parameters of the problem, and thus gives a dual symbolic-numeric finite element environment and produces a solution in terms of multivariate power series expansion. Zhao et al. [3] derived analytical solutions in a 3D anisotropic magnetoelectroelastic bimaterial space subject to uniform extended dislocations and tractions within a horizontal circular area.

The analytical Green's function solution is important in micromechanics. Pouya [4] put forward an accurate definition for ellipsoidal anisotropy and provide an explicit nondegenerate Green's function solution. Yuan and Yin [5] proposed the elastic Green's function for a functional graded material. Franciosi et al. [6] proposed an analytical solution for the mean and axial Green operators of circular cylindrical inclusions with finite length in 3D isotropic materials. Franciosi [7] proposed a generic Green operator-based analytical solution form for all the effective generalized elastic-like moduli of n-phase lami-

* Corresponding author.
E-mail address: yuanzifeng@pku.edu.cn (Z. Yuan).

https://doi.org/10.1016/j.taml.2025.100618
Received 13 June 2025; Received in revised form 15 September 2025; Accepted 15 September 2025
Available online 18 September 2025

nates. Shang et al. [8] derived an analytical solution of multilayered structures with Green's function. The reduced-order-homogenization [9–11] is constructed via numerical Green's function or so-called influence functions, which can be derived analytically as well [12].

In linear elastic fracture mechanics, analytical solutions of the linear elastic boundary value problem can be used to derive stress intensity factors (SIFs); thus, various mathematical models are introduced in deriving closed-form solutions for a domain with a crack tip. Thube and Gotkhindi [13] proposed a hybrid FE-analytical method based on the WILLIAMS series to obtain the SIF and higher-order coefficients. Sun and Xiang [14] proposed a semianalytical SIF around an elliptical notch. Xing et al. [15] provide an analytical model to calculate the stress fields around sharp V-shaped notches in plates so that the SIF can be derived analytically. Pistorio et al. [16] proposed a closed-form expression for the SIF around the cracks in lithium ion batteries.

The linear homogenization problem aims to derive macro-scopic effective properties with given unit cell geometry and phase material properties. Usually, the homogenized properties are obtained by solving a unit cell problem numerically. For some specific unit cells, an analytical solution can be found with proper assumptions. For example, Li et al. [17,18] presented an analytical homogenization method in terms of trigonometric function series and obtain effective properties of honeycomb sandwiches plates with skin and height effects. Bartolozzi et al. [19] perform an experimental campaign to validate analytical homogenization models for corrugated core sandwich panels. Kalisch and Glüge [20] obtained analytical expressions for the effective stiffness of laminate with various types of elastic models. Shakiba et al. [21] presented an analytic differentiation method to obtain the sensitivity of the transverse failure response of carbon fiber composite laminates to the distribution parameters of the fiber/matrix interface properties. Heide-Jorgensen [22] studied the through-the-thickness diffusivity problem for plain-woven composite and proposed an analytical homogenization scheme. Huang et al. [23] derived an analytical homogenization scheme for equivalent in-plane elastic moduli of multimaterial honeycombs. Guo et al. [24] derived the equivalent in-plane elastic moduli of prestressed lattices based on the micropolar elasticity model analytically. Huang et al. [25] adopted the Eshelby tensor to evaluate the maximum effective stress at the interface.

Analytical elastic solutions are essential for the boundary element method (BEM). Salvadori [26] proposed a closed-form of the integrals from both the standard (collocation) BEM and the symmetric GALERKIN BEM. Shiah [27] proposed an analytical method to transform the volume integral to surface ones for the body-force effect in 3D anisotropic elasticity. Krome and Gravenkamp [28] proposed a semianalytical formulation for the simulation and modeling of curved structures based on the scaled boundary finite element method.

Marmo and Rosati [29] presented an analytical integration of elasto-plastic uniaxial constitutive laws polygonal sections of arbitrary sections. Hospital-Bravo et al. [30] constructed a semi-analytical scheme for highly oscillatory integrals over the tetrahedron domain. Analytical solutions can also be used to verify numerical methods. Miled et al. [31] provides analytical integration for the verification problem (uniaxial tension and simple shear) of viscoelastic-viscoplastic constitutive model. Cervera et al. [32] proposed the strain localization analysis of Hill's orthotropic plasticity and the method is verified analytically.

In this manuscript, we propose a novel methodology to obtain an approximate analytical solution for an isotropic homogeneous elastic medium. The elastic domain can be arbitrary but needs to be discretized with finite element mesh. The approximate analytical solution is given by solving a special linear finite element problem and finally expressed into a series in terms of Poisson's ratio. We name this method computational method for analytical solutions with finite element (CMAS-FE). CMAS-FE provides an offline problem-handling technique. With the same finite element mesh, when material parameters are modified online, the mechanical quantities can be obtained at a certain degree of freedom or a certain integration point with a time complexity of $O(1)$.

This manuscript is organized as follows. Section 2 first reviews the governing equations of linear elasticity and numerical method with the linear finite element method, and introduces detailed derivations of the CMAS-FE method. Next, Section 3 introduces two numerical examples to verify the CMAS-FE method, especially the convergence of the method. Section 4 provides two extra applications of the CMAS-FE method. Finally, conclusions are given in Section 5.

2. Methodology

In this section, we first briefly review the governing equations for the linear elastic problem as well as the linear finite element method (LFEM) in Section 2.1. Next, we introduce a special decomposition of isotropic elastic stiffness tensor and apply it to the LFEM in Section 2.2. At last, we introduce a procedure to obtain an approximate analytical solution by solving a special system of linear equations assembled by the LFEM in Section 2.3.

2.1. Brief review of linear elastic problem with linear finite element method (LFEM)

Assume $\Omega \subset (\mathbb{R})^3$ is a homogeneous elastic domain with a uniform Young's modulus E and Poisson's ratio ν. The governing equations for this linear elastic problem are written as the following:

$$\begin{cases} \sigma_{ij,j} + b_i = 0, & \text{for } \boldsymbol{x} \in \Omega, \\ \sigma_{ij} = \lambda \varepsilon_{kk}\delta_{ij} + 2\mu\varepsilon_{ij}, & \text{for } \boldsymbol{x} \in \Omega, \\ \varepsilon_{ij} = \left(u_{i,j} + u_{j,i}\right)/2, & \text{for } \boldsymbol{x} \in \Omega, \\ u_i = \bar{u}_i, & \text{for } \boldsymbol{x} \in \Gamma_{\mathrm{c}}, \\ \sigma_{ij} n_j = \bar{t}_i, & \text{for } \boldsymbol{x} \in \Gamma_{\mathrm{t}}, \end{cases} \tag{1}$$

with u_i represents the displacements, ε_{ij} denotes the strains, σ_{ij} represents the stresses, b_i represents the body forces, $\bar{u}_i$ the prescribed displacement, $\bar{t}_i$ represents the prescribed traction force, Γ_{c} the boundary domain for the essential boundary condition, Γ_{t} the boundary domain for the nature boundary condition, where $\Gamma_{\mathrm{t}} \cap \Gamma_{\mathrm{c}} = \varnothing$, $\Gamma_{\mathrm{t}} \cup \Gamma_{\mathrm{c}} = \Gamma \equiv \partial\Omega$. λ and μ are LAMÉ constants with

$$\lambda = \frac{E\,\nu}{(1-2\nu)(1+\nu)}, \mu = \frac{E}{2(1+\nu)}. \tag{2}$$

There are numerous closed-form analytical solutions in terms of elementary functions in history. Nonetheless, when the domain Ω is complex, obtaining an analytical solution becomes challenging. The linear finite element method (LFEM) has been proven to be an effective and accurate method for obtaining an approximate solution for the equations Eq. (1). In the LFEM, the domain Ω is discretized into subdomains named "elements" where $\Omega = \cup_e \Omega^e$, Ω^e denotes the domain for eth element. Notably, in this manuscript, "element" refers to a solid or continuum element, rather than a structural element such as a beam or shell. Within one solid element, one can evaluate the so-called element stiffness matrix $\boldsymbol{K}^e$ such that

$$\boldsymbol{K}^e = \sum_{\mathrm{I}} \boldsymbol{B}_{\mathrm{I}}^{\mathrm{T}} \{\mathbb{L}\} \boldsymbol{B}_{\mathrm{I}} |\boldsymbol{J}_{\mathrm{I}}| w_{\mathrm{I}}, \tag{3}$$

where subscription "I" denotes the index of the quadrature point, $\boldsymbol{B}_{\mathrm{I}}$ represents the strain-displacement matrix which interpolates strain by the elemental displacement vector, $\boldsymbol{J}_{\mathrm{I}}$ is the JACOBIAN matrix defined as $\boldsymbol{J} \equiv \partial \boldsymbol{x}/\partial \boldsymbol{\xi}$, and $\boldsymbol{\xi}$ represents the isoparametric coordinates. The parameter w_{I} represents the quadrature weight, and

$$\{\mathbb{L}\} = \begin{bmatrix} \lambda+2\mu & \lambda & \lambda & & & \\ \lambda & \lambda+2\mu & \lambda & & & \\ \lambda & \lambda & \lambda+2\mu & & & \\ & & & \mu & & \\ & & & & \mu & \\ & & & & & \mu \end{bmatrix} \tag{4}$$

is the elastic stiffness tensor in VOIGT notation $\{\cdot\}$.

With given nodal connectivity of all the elements, we can assemble the global stiffness matrix $\boldsymbol{K}$, and we may solve the following sparse linear equation systems to obtain displacements that

$$\begin{bmatrix} \boldsymbol{K}_{\mathrm{uu}} & \boldsymbol{K}_{\mathrm{uc}} \\ \boldsymbol{K}_{\mathrm{uc}}^{\mathrm{T}} & \boldsymbol{K}_{\mathrm{cc}} \end{bmatrix} \begin{bmatrix} \boldsymbol{d} \\ \bar{\boldsymbol{u}} \end{bmatrix} = \begin{bmatrix} \boldsymbol{f} \\ \boldsymbol{r}+\bar{\boldsymbol{f}} \end{bmatrix}, \tag{5}$$

where $\boldsymbol{d}$ is the displacements to solve; $\bar{\boldsymbol{u}}$ denotes the constraint displacements; $\boldsymbol{f}$ and $\bar{\boldsymbol{f}}$ are the prescribed nodal forces at unknown and constraint displacement degrees-of-freedom, respectively; and $\boldsymbol{r}$ are the reaction forces at the constraint displacements. Thus, one can construct the linear equations respect to $\boldsymbol{d}$ that

$$\boldsymbol{K}_{\mathrm{uu}}\boldsymbol{d} = \boldsymbol{f} - \boldsymbol{K}_{\mathrm{uc}}\bar{\boldsymbol{u}}, \Rightarrow \boldsymbol{d} = \boldsymbol{K}_{\mathrm{uu}}^{-1}\left(\boldsymbol{f} - \boldsymbol{K}_{\mathrm{uc}}\bar{\boldsymbol{u}}\right). \tag{6}$$

Once rigid-body motions and rotations are constrained by proper essential boundary conditions, there will be a unique solution for $\boldsymbol{d}$.

2.2. Decomposition of the isotropic elastic stiffness tensor

Under the framework of the LFEM, we aim to derive the element stiffness and then the global stiffness matrix in terms of material parameters. We first rewrite the isotropic elastic stiffness tensor Eq. (4) into

$$\begin{aligned} \{\mathbb{L}\} &= \frac{E}{(1-2\nu)(1+\nu)} \begin{bmatrix} 1-\nu & \nu & \nu & & & & \\ \nu & 1-\nu & \nu & & & & \\ \nu & \nu & 1-\nu & & & & \\ & & & 0.5-\nu & & & \\ & & & & 0.5-\nu & & \\ & & & & & 0.5-\nu & \end{bmatrix} \\ &= \frac{E}{(1-2\nu)(1+\nu)} \left[\boldsymbol{H}_0 - \left(\nu+\tfrac{1}{4}\right)\boldsymbol{H}_1\right], \end{aligned} \tag{7}$$

where

$$\boldsymbol{H}_0 = \begin{bmatrix} 5/4 & -1/4 & -1/4 & & & & \\ -1/4 & 5/4 & -1/4 & & & & \\ -1/4 & -1/4 & 5/4 & & & & \\ & & & 3/4 & & & \\ & & & & 3/4 & & \\ & & & & & 3/4 & \end{bmatrix},$$

$$\boldsymbol{H}_1 = \begin{bmatrix} 1 & -1 & -1 & & & & \\ -1 & 1 & -1 & & & & \\ -1 & -1 & 1 & & & & \\ & & & 1 & & & \\ & & & & 1 & & \\ & & & & & 1 & \end{bmatrix}. \tag{8}$$

Clearly, $\boldsymbol{H}_0$ is symmetric and positive-definite, whereas $\boldsymbol{H}_1$ is symmetric only. We also have

$$\left(\boldsymbol{H}_0^{-1}\boldsymbol{H}_1\right)^2 = \frac{16}{9}\boldsymbol{I}. \tag{9}$$

In addition, we can evaluate the spectral radius that

$$\rho\left[\left(\nu+\frac{1}{4}\right)\boldsymbol{H}_0^{-1}\boldsymbol{H}_1\right] = \left|\nu+\frac{1}{4}\right|\rho\left(\boldsymbol{H}_0^{-1}\boldsymbol{H}_1\right) = \left|\nu+\frac{1}{4}\right|\cdot\frac{4}{3} < 1, \tag{10}$$

since the Poisson's ratio $\nu \in (-1, 0.5)$, where $\rho(\boldsymbol{A})$ denotes the spectral radius of a matrix $\boldsymbol{A}$. Here we define a so-called shifted Poisson's ratio ϖ such that

$$\varpi \equiv \nu + \frac{1}{4} \in (-3/4, +3/4), \Rightarrow (1-2\nu)(1+\nu) = \frac{9}{8} - 2\varpi^2 \in (0, 9/8] \tag{11}$$

to simplify the expression. Thus, we have

$$\begin{aligned} \{\mathbb{L}\}^{-1} &= \frac{9/8-2\varpi^2}{E}\left[\boldsymbol{I} - \varpi\boldsymbol{H}_0^{-1}\boldsymbol{H}_1\right]^{-1}\boldsymbol{H}_0^{-1} \\ &= \frac{9/8-2\varpi^2}{E}\left[\boldsymbol{I} + \textstyle\sum_{k=1}^{\infty}\varpi^k\left(\boldsymbol{H}_0^{-1}\boldsymbol{H}_1\right)^k\right]\boldsymbol{H}_0^{-1} \\ &= \frac{9/8-2\varpi^2}{E}\frac{\varpi\boldsymbol{H}_0^{-1}\boldsymbol{H}_1 + \boldsymbol{I}}{1-\varpi^2\cdot 16/9}\boldsymbol{H}_0^{-1} = \{\mathbb{M}\}, \end{aligned} \tag{12}$$

where $\mathbb{M}$ denotes the linear elastic compliance tensor. Then the element stiffness matrix is written as

$$\boldsymbol{K}^e = \frac{E}{9/8-2\varpi^2}\sum\nolimits_{\mathrm{I}}\boldsymbol{B}_{\mathrm{I}}^{\mathrm{T}}\left[\boldsymbol{H}_0 - \varpi\boldsymbol{H}_1\right]\boldsymbol{B}_{\mathrm{I}}|\boldsymbol{J}_{\mathrm{I}}|w_{\mathrm{I}} = \frac{E}{9/8-2\varpi^2}\left[\boldsymbol{R}_0^e - \varpi\boldsymbol{R}_1^e\right], \tag{13}$$

with

$$\boldsymbol{R}_0^e \equiv \sum\nolimits_{\mathrm{I}}\boldsymbol{B}_{\mathrm{I}}^{\mathrm{T}}\boldsymbol{H}_0\boldsymbol{B}_{\mathrm{I}}|\boldsymbol{J}_{\mathrm{I}}|w_{\mathrm{I}}, \boldsymbol{R}_1^e \equiv \sum\nolimits_{\mathrm{I}}\boldsymbol{B}_{\mathrm{I}}^{\mathrm{T}}\boldsymbol{H}_1\boldsymbol{B}_{\mathrm{I}}|\boldsymbol{J}_{\mathrm{I}}|w_{\mathrm{I}}. \tag{14}$$

Both $\boldsymbol{R}_0^e$ and $\boldsymbol{R}_1^e$ depend only on the nodal coordinates of this element but irrelevant to elastic parameters. In addition, both $\boldsymbol{R}_0^e$ and $\boldsymbol{R}_1^e$ have the same matrix dimension as $\boldsymbol{K}^e$, and the dimensions of both $\boldsymbol{R}_0^e$ and $\boldsymbol{R}_1^e$ are length [L].

2.3. Deriving an approximate analytical solution through the LFEM

One can assemble the corresponding global matrix Eq. (5) with $\boldsymbol{R}_0$ and $\boldsymbol{R}_1$ such that

$$\frac{E}{9/8-2\varpi^2}\begin{bmatrix} \boldsymbol{R}_{0,\mathrm{uu}} - \varpi\boldsymbol{R}_{1,\mathrm{uu}} & \boldsymbol{R}_{0,\mathrm{uc}} - \varpi\boldsymbol{R}_{1,\mathrm{uc}} \\ \boldsymbol{R}_{0,\mathrm{uc}}^{\mathrm{T}} - \varpi\boldsymbol{R}_{1,\mathrm{uc}}^{\mathrm{T}} & \boldsymbol{R}_{0,\mathrm{cc}} - \varpi\boldsymbol{R}_{1,\mathrm{cc}} \end{bmatrix}\begin{bmatrix} \boldsymbol{d} \\ \bar{\boldsymbol{u}} \end{bmatrix} = \begin{bmatrix} \boldsymbol{f} \\ \boldsymbol{r}+\bar{\boldsymbol{f}} \end{bmatrix}. \tag{15}$$

Thus, Eq. (6) can be rewritten with respect to $\boldsymbol{R}_0$ and $\boldsymbol{R}_1$ such that

$$\frac{E}{9/8-2\varpi^2}\left[\boldsymbol{R}_{0,\mathrm{uu}} - \varpi\boldsymbol{R}_{1,\mathrm{uu}}\right]\boldsymbol{d} = \boldsymbol{f} - \frac{E}{9/8-2\varpi^2}\left[\boldsymbol{R}_{0,\mathrm{uc}} - \varpi\boldsymbol{R}_{1,\mathrm{uc}}\right]\bar{\boldsymbol{u}}, \tag{16}$$

or

$$\left[\boldsymbol{R}_{0,\mathrm{uu}} - \varpi\boldsymbol{R}_{1,\mathrm{uu}}\right]\boldsymbol{d} = \frac{9/8-2\varpi^2}{E}\boldsymbol{f} - \left[\boldsymbol{R}_{0,\mathrm{uc}} - \varpi\boldsymbol{R}_{1,\mathrm{uc}}\right]\bar{\boldsymbol{u}}. \tag{17}$$

Again that $\boldsymbol{R}_{0,\mathrm{uu}}$, $\boldsymbol{R}_{1,\mathrm{uu}}$, $\boldsymbol{R}_{0,\mathrm{uc}}$, and $\boldsymbol{R}_{1,\mathrm{uc}}$ are matrices that depends on the finite element mesh only and irrelevant to the material parameters. In other words, one can evaluate these matrices with a given finite element mesh and essential boundary Γ_{c}. In addition, if $\boldsymbol{K}_{\mathrm{uu}}$ is invertible, we also have $\boldsymbol{R}_{0,\mathrm{uu}}$ as invertible.

Similarly, we have

$$\left[\boldsymbol{R}_{0,\mathrm{uu}} - \varpi\boldsymbol{R}_{1,\mathrm{uu}}\right]^{-1} = \left[\boldsymbol{I} + \sum_{k=1}^{\infty}\varpi^k\left(\boldsymbol{R}_{0,\mathrm{uu}}^{-1}\boldsymbol{R}_{1,\mathrm{uu}}\right)^k\right]\boldsymbol{R}_{0,\mathrm{uu}}^{-1}. \tag{18}$$

The displacement solution is then given as

$$\boldsymbol{d} = \left[\boldsymbol{I} + \sum_{k=1}^{\infty}\varpi^k\left(\boldsymbol{R}_{0,\mathrm{uu}}^{-1}\boldsymbol{R}_{1,\mathrm{uu}}\right)^k\right]\boldsymbol{R}_{0,\mathrm{uu}}^{-1}\left[\frac{9/8-2\varpi^2}{E}\boldsymbol{f} - \left(\boldsymbol{R}_{0,\mathrm{uc}} - \varpi\boldsymbol{R}_{1,\mathrm{uc}}\right)\bar{\boldsymbol{u}}\right]. \tag{19}$$

We can rearrange the solution into the following series form:

$$\boldsymbol{d} = \sum_{k=0}^{\infty}\varpi^k\left(\boldsymbol{a}_k + \frac{\boldsymbol{b}_k}{E}\right), \text{or } d_I = \sum_{k=0}^{\infty}\varpi^k\left(a_{I,k} + \frac{b_{I,k}}{E}\right), \tag{20}$$

with

$$\begin{aligned} \boldsymbol{a}_0 &= \boldsymbol{R}_{0,\mathrm{uu}}^{-1}\left(-\boldsymbol{R}_{0,\mathrm{uc}}\,\bar{\boldsymbol{u}}\right), \\ \boldsymbol{a}_1 &= \boldsymbol{R}_{0,\mathrm{uu}}^{-1}\left(\boldsymbol{R}_{1,\mathrm{uu}}\boldsymbol{a}_0 + \boldsymbol{R}_{1,\mathrm{uc}}\bar{\boldsymbol{u}}\right), \\ \boldsymbol{a}_k &= \boldsymbol{R}_{0,\mathrm{uu}}^{-1}\left(\boldsymbol{R}_{1,\mathrm{uu}}\boldsymbol{a}_{k-1}\right), k = 2, 3, \ldots \end{aligned} \tag{21}$$

and

$$\begin{aligned} \boldsymbol{b}_0 &= \boldsymbol{R}_{0,\mathrm{uu}}^{-1}\left(\frac{9}{8}\boldsymbol{f}\right), \\ \boldsymbol{b}_1 &= \boldsymbol{R}_{0,\mathrm{uu}}^{-1}\left(\boldsymbol{R}_{1,\mathrm{uu}}\boldsymbol{b}_0\right), \\ \boldsymbol{b}_2 &= \boldsymbol{R}_{0,\mathrm{uu}}^{-1}\left(\boldsymbol{R}_{1,\mathrm{uu}}\boldsymbol{b}_1 - 2\boldsymbol{f}\right), \\ \boldsymbol{b}_k &= \boldsymbol{R}_{0,\mathrm{uu}}^{-1}\left(\boldsymbol{R}_{1,\mathrm{uu}}\boldsymbol{b}_{k-1}\right), k = 3, 4, \ldots \end{aligned} \tag{22}$$

The dimensions of $\boldsymbol{a}_k$ and $\boldsymbol{b}_k$ are length [L] and force per length [F/L], respectively. In the numerical implementation, it is recommended to solve $\boldsymbol{a}_0$, $\boldsymbol{a}_1$, … sequentially as well as $\boldsymbol{b}_0$, $\boldsymbol{b}_1$, …. All the coefficient vectors $\boldsymbol{a}_k$ and $\boldsymbol{b}_k$ are solved by the same coefficient matrix $\boldsymbol{R}_{0,\mathrm{uu}}$. During the numerical implementation, one may store a proper matrix factorization of $\boldsymbol{R}_{0,\mathrm{uu}}$ in memory to avoid repetitive matrix factorization.

We may continue to evaluate strain and stress tensors at one quadrature point such that

$$\{\boldsymbol{\varepsilon}_{\mathrm{I}}^{e}\} = \boldsymbol{B}_{\mathrm{I}}\boldsymbol{d}^{e} = \sum_{k=0}^{\infty}\varpi^{k}\left(\boldsymbol{B}_{\mathrm{I}}\boldsymbol{a}_{k}^{e} + \frac{\boldsymbol{B}_{\mathrm{I}}\boldsymbol{b}_{k}^{e}}{E}\right), \tag{23}$$

where $\boldsymbol{d}^{e}$ is the element displacement vector. Alternatively, we can rewrite Eq. (23) in matrix form such that

$$\{\boldsymbol{\varepsilon}_{\mathrm{I}}^{e}\} = \boldsymbol{B}_{\mathrm{I}}\left\{\begin{bmatrix} a_{1,0}^{e} & a_{1,1}^{e} & a_{1,2}^{e} & \cdots \\ a_{2,0}^{e} & a_{2,1}^{e} & a_{2,2}^{e} & \cdots \\ \vdots & \vdots & \vdots & \ddots \\ a_{n,0}^{e} & a_{n,1}^{e} & a_{n,2}^{e} & \cdots \end{bmatrix} + \frac{1}{E}\begin{bmatrix} b_{1,0}^{e} & b_{1,1}^{e} & b_{1,2}^{e} & \cdots \\ b_{2,0}^{e} & b_{2,1}^{e} & b_{2,2}^{e} & \cdots \\ \vdots & \vdots & \vdots & \ddots \\ b_{n,0}^{e} & b_{n,1}^{e} & b_{n,2}^{e} & \cdots \end{bmatrix}\right\}\begin{bmatrix} 1 \\ \varpi \\ \varpi^{2} \\ \vdots \end{bmatrix}, \tag{24}$$

where n denotes the number of elemental degrees-of-freedom. The stress tensor is then evaluated by

$$\begin{aligned}\{\boldsymbol{\sigma}_{\mathrm{I}}^{e}\} &= \frac{E}{9/8 - 2\varpi^{2}}\left[\boldsymbol{H}_{0} - \varpi\boldsymbol{H}_{1}\right]\{\boldsymbol{\varepsilon}_{\mathrm{I}}^{e}\} \\ &= \frac{E}{9/8 - 2\varpi^{2}}\left[\boldsymbol{H}_{0} - \varpi\boldsymbol{H}_{1}\right]\sum_{k=0}^{\infty}\varpi^{k}\left(\boldsymbol{B}_{\mathrm{I}}\boldsymbol{a}_{k}^{e} + \frac{\boldsymbol{B}_{\mathrm{I}}\boldsymbol{b}_{k}^{e}}{E}\right).\end{aligned} \tag{25}$$

We may also obtain the reaction force at constraint degrees-of-freedom by

$$\begin{aligned}\boldsymbol{r} &= \frac{E}{9/8 - 2\varpi^{2}}\left[\boldsymbol{R}_{0,\mathrm{uc}}^{\mathrm{T}} - \varpi\boldsymbol{R}_{1,\mathrm{uc}}^{\mathrm{T}}\right]\boldsymbol{d} + \frac{E}{9/8 - 2\varpi^{2}}\left[\boldsymbol{R}_{0,\mathrm{cc}} - \varpi\boldsymbol{R}_{1,\mathrm{cc}}\right]\bar{\boldsymbol{u}} - \bar{\boldsymbol{f}} \\ &= \frac{E}{9/8 - 2\varpi^{2}}\left\{\left[\boldsymbol{R}_{0,\mathrm{uc}}^{\mathrm{T}} - \varpi\boldsymbol{R}_{1,\mathrm{uc}}^{\mathrm{T}}\right]\sum_{k=0}^{\infty}\varpi^{k}\left(\boldsymbol{a}_{k} + \frac{\boldsymbol{b}_{k}}{E}\right) + \left[\boldsymbol{R}_{0,\mathrm{cc}} - \varpi\boldsymbol{R}_{1,\mathrm{cc}}\right]\bar{\boldsymbol{u}}\right\} - \bar{\boldsymbol{f}}.\end{aligned} \tag{26}$$

Consequently, the strains and stresses at the quadrature points as well as the reaction force at constraint degrees-of-freedom can be interpreted with series with different orders of ϖ such as Eq. (20).

The shifted Poisson's ratio may not be straightforward enough to express the various types of solutions. Thus, we can finally rewrite Eq. (20) into a series solution on the basis of various orders of Poisson's ratio such that:

$$\boldsymbol{d} = \sum_{k=0}^{\infty}\nu^{k}\left(\tilde{\boldsymbol{a}}_{k} + \frac{\tilde{\boldsymbol{b}}_{k}}{E}\right), \text{or } d_{I} = \sum_{k=0}^{\infty}\nu^{k}\left(\tilde{a}_{I,k} + \frac{\tilde{b}_{I,k}}{E}\right). \tag{27}$$

Similarly, the strains at the quadrature point are

$$\{\boldsymbol{\varepsilon}_{\mathrm{I}}^{e}\} = \boldsymbol{B}_{\mathrm{I}}\boldsymbol{d}^{e} = \sum_{k=0}^{\infty}\nu^{k}\left(\boldsymbol{B}_{\mathrm{I}}\tilde{\boldsymbol{a}}_{k}^{e} + \frac{\boldsymbol{B}_{\mathrm{I}}\tilde{\boldsymbol{b}}_{k}^{e}}{E}\right), \tag{28}$$

while the stresses are rearranged into

$$\begin{aligned}\{\boldsymbol{\sigma}_{\mathrm{I}}^{e}\} &= \frac{E}{(1-2\nu)(1+\nu)}\left[(\boldsymbol{H}_{0} - \boldsymbol{H}_{1}/4) - \nu\boldsymbol{H}_{1}\right]\sum_{k=0}^{\infty}\nu^{k}\left(\boldsymbol{B}_{\mathrm{I}}\tilde{\boldsymbol{a}}_{k}^{e} + \frac{\boldsymbol{B}_{\mathrm{I}}\tilde{\boldsymbol{b}}_{k}^{e}}{E}\right) \\ &= \frac{E}{(1-2\nu)(1+\nu)}\sum_{k=0}^{\infty}\nu^{k}\left[(\boldsymbol{H}_{0} - \boldsymbol{H}_{1}/4)\boldsymbol{B}_{\mathrm{I}}\tilde{\boldsymbol{a}}_{k}^{e} - \boldsymbol{H}_{1}\boldsymbol{B}_{\mathrm{I}}\tilde{\boldsymbol{a}}_{k-1}^{e}\right] \\ &\quad + \frac{1}{(1-2\nu)(1+\nu)}\sum_{k=0}^{\infty}\nu^{k}\left[(\boldsymbol{H}_{0} - \boldsymbol{H}_{1}/4)\boldsymbol{B}_{\mathrm{I}}\tilde{\boldsymbol{b}}_{k}^{e} - \boldsymbol{H}_{1}\boldsymbol{B}_{\mathrm{I}}\tilde{\boldsymbol{b}}_{k-1}^{e}\right],\end{aligned} \tag{29}$$

with $\tilde{\boldsymbol{a}}_{-1}^{e} = \boldsymbol{0}$, $\tilde{\boldsymbol{b}}_{-1}^{e} = \boldsymbol{0}$. The reaction forces as follows:

$$\begin{aligned}\boldsymbol{r} &= \frac{E}{(1-2\nu)(1+\nu)}\left[(\boldsymbol{R}_{0,\mathrm{uc}}^{\mathrm{T}} - \boldsymbol{R}_{1,\mathrm{uc}}^{\mathrm{T}}/4) - \nu\boldsymbol{R}_{1,\mathrm{uc}}^{\mathrm{T}}\right]\sum_{k=0}^{\infty}\nu^{k}\left(\tilde{\boldsymbol{a}}_{k} + \frac{\tilde{\boldsymbol{b}}_{k}}{E}\right) \\ &\quad + \frac{E}{(1-2\nu)(1+\nu)}\left[(\boldsymbol{R}_{0,\mathrm{cc}} - \boldsymbol{R}_{1,\mathrm{cc}}/4) - \nu\boldsymbol{R}_{1,\mathrm{cc}}\right]\bar{\boldsymbol{u}} - \bar{\boldsymbol{f}} \\ &= \frac{E}{(1-2\nu)(1+\nu)}\sum_{k=0}^{\infty}\nu^{k}\left[(\boldsymbol{R}_{0,\mathrm{uc}}^{\mathrm{T}} - \boldsymbol{R}_{1,\mathrm{uc}}^{\mathrm{T}}/4)\tilde{\boldsymbol{a}}_{k} - \boldsymbol{R}_{1,\mathrm{uc}}^{\mathrm{T}}\tilde{\boldsymbol{a}}_{k-1}\right] \\ &\quad + \frac{E}{(1-2\nu)(1+\nu)}\left[(\boldsymbol{R}_{0,\mathrm{cc}} - \boldsymbol{R}_{1,\mathrm{cc}}/4) - \nu\boldsymbol{R}_{1,\mathrm{cc}}\right]\bar{\boldsymbol{u}} \\ &\quad + \frac{1}{(1-2\nu)(1+\nu)}\sum_{k=0}^{\infty}\nu^{k}\left[(\boldsymbol{R}_{0,\mathrm{uc}}^{\mathrm{T}} - \boldsymbol{R}_{1,\mathrm{uc}}^{\mathrm{T}}/4)\tilde{\boldsymbol{b}}_{k} - \boldsymbol{R}_{1,\mathrm{uc}}^{\mathrm{T}}\tilde{\boldsymbol{b}}_{k-1}\right] - \bar{\boldsymbol{f}}.\end{aligned} \tag{30}$$

In practice, we may prefer a truncated solution with a finite number of terms of different orders of the Poisson's ratio. We define

$$\boldsymbol{d}_{N} = \sum_{k=0}^{N}\nu^{k}\left(\tilde{\boldsymbol{a}}_{k} + \frac{\tilde{\boldsymbol{b}}_{k}}{E}\right), \tag{31}$$

and the truncated strains, stresses, and reaction forces can be defined in the same manner.

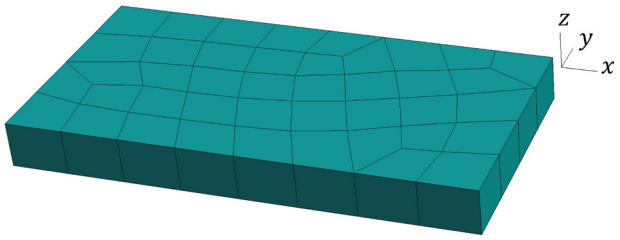

Fig. 1. Finite element mesh with 8-node hexahedron elements for the patch test.

3. Numerical verification

In this section, four groups of numerical examples are conducted to validate the method through comparison of the approximated analytical solution with respect to the numerical results of the LFEM.

3.1. Patch test

We start with a patch test to verify whether an exact analytical solution can be derived. We use 8-node hexahedron element with full integration scheme to mesh the plate as depicted in Fig. 1. We define the length (along the x axis), width (along the y axis), and height (along the z axis) as $a = 2$, $b = 1$, and $h = 0.2$, respectively. We assign $u = 0$ at the surface $x = 0$; $v = 0$ at the surface $y = 0$; $w = 0$ at the surface $z = 0$; and $u = \bar{u} = 0.01$ at the surface $x = a = 2$.

The patch test gives uniform strains and stresses over the whole domain

$$\begin{aligned}&\varepsilon_{11} = \frac{\bar{u}}{a}, \varepsilon_{22} = \varepsilon_{33} = -\nu\frac{\bar{u}}{a}, \varepsilon_{ij} = 0, \text{for } ij = 23, 13, 12, \\ &\sigma_{11} = E\frac{\bar{u}}{a}, \sigma_{ij} = 0, \text{for } ij = 22, 33, 23, 13, 12,\end{aligned} \tag{32}$$

and linearly distributed the displacement field such that

$$u(x,y,z) = \underbrace{\frac{\bar{u}}{a}x}_{\tilde{\boldsymbol{a}}_{0}\text{ term}}; v(x,y,z) = \underbrace{\nu\left(-\frac{\bar{u}}{a}y\right)}_{\tilde{\boldsymbol{a}}_{1}\text{ term}}; w(x,y,z) = \underbrace{\nu\left(-\frac{\bar{u}}{a}z\right)}_{\tilde{\boldsymbol{a}}_{1}\text{ term}}. \tag{33}$$

Consequently, there are only two nonzero terms $\tilde{\boldsymbol{a}}_{0}$ and $\tilde{\boldsymbol{a}}_{1}$ for the approximated analytical solution $\boldsymbol{d}$, and match the numerical results. We may plot the values of $\tilde{\boldsymbol{a}}_{0}$ and $\tilde{\boldsymbol{a}}_{1}$ for displacement u, v, and w with respect to x, y, and z, respectively, as depicted in Fig. 2.

3.2. Pure-bending test

We continue to derive an approximate analytical solution for a pure-bending problem depicted in Fig. 3. The length, width, and height of the beam are L, b, and h, respectively. The beam is meshed by 8-node hexahedron elements.

We consider a beam with size $L = 4$, and $h = 2$. Thus, this beam actually is not a typical slender beam structure. Here we use cubic-shaped 8-node hexahedron element to mesh the beam with element size $l_{\mathrm{el}} = 1/4$, $1/8$, and $1/16$. We set the width as the element size $b = 2l_{\mathrm{el}}$, and keep $M_{y}/b = 2$, where M_{y} is the moment about the y axis. The CMAS-FE is then able to evaluate the coefficients $\tilde{\boldsymbol{a}}_{k}$ and $\tilde{\boldsymbol{b}}_{k}$, $k = 0, 1, \ldots$ for each problem.

We first study how the truncated solution $\boldsymbol{d}_{N}$ converges to the reference solution via the LFEM named the $\boldsymbol{d}_{\mathrm{LFEM}}$ as N increases, which can be marked as series-convergence. Because the LFEM requires values of Young's modulus and Poisson's ratio rather than symbols; we assign $E = 2.1 \times 10^{5}$ MPa and $\nu = 0.23$. Accordingly, we can obtain numerical values of each $\boldsymbol{d}_{N}$ and compare it with the $\boldsymbol{d}_{\mathrm{LFEM}}$. We take the case $l_{\mathrm{el}} = 1/8$ as an example. Fig. 4(b)–(d) depicts the errors between

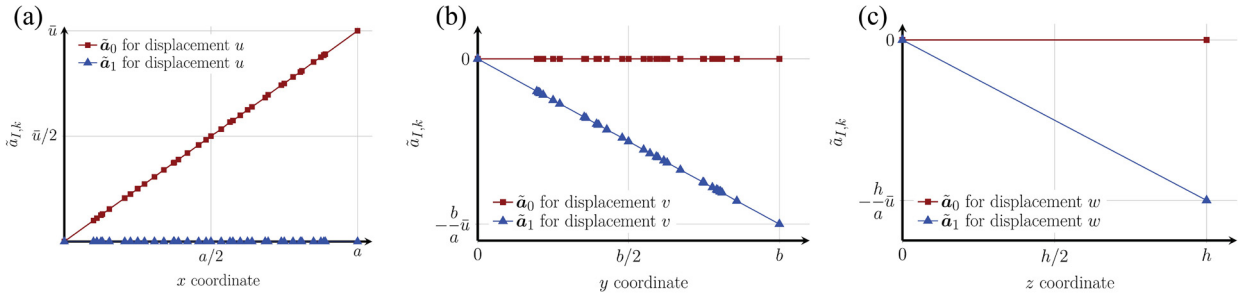

Fig. 2. Verification of $\tilde{\boldsymbol{a}}_0$ and $\tilde{\boldsymbol{a}}_1$ for: (a) displacement u; (b) displacement v; (c) displacement w at all nodes.

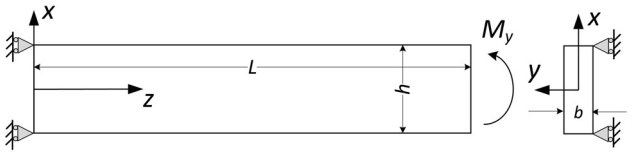

Fig. 3. Sketch of the pure-bending problem.

$\boldsymbol{d}_0 - \boldsymbol{d}_{\text{LFEM}}$, $\boldsymbol{d}_1 - \boldsymbol{d}_{\text{LFEM}}$, and $\boldsymbol{d}_2 - \boldsymbol{d}_{\text{LFEM}}$, respectively, while the reference solution $\boldsymbol{d}_{\text{LFEM}}$ is depicted in Fig. 4(a). Clearly the error decreases to a very small even N only reaches 2 except around the corner regions. Similar observations can be found for the truncated strain and stress fields, which are depicted in Figs. 5 and 6, respectively.

The mesh convergence can also be observed in Fig. 7, where the error between $\boldsymbol{d}_N$, $N = 0, 1, 2$ and the reference solutions $\boldsymbol{d}_{\text{LFEM}}$ with element sizes of $l_{\text{el}} = 1/4$, $1/8$, and $1/16$ are depicted. We can see that the magnitude of errors is reduced by the mesh refinement or the increasing number of truncated terms. Furthermore, the relative errors of the displacement, strain, and stress fields with increasing number of truncated terms N are plotted in Fig. 8(a)–(c), respectively.

Finally, there is an analytical solution for a pure-bending problem even when the beam is not a typical slender beam that

$$\begin{aligned} u &= -\frac{M_y}{2EI_y}[-z^2 + \nu(y^2 - x^2)] = \left[\frac{M_y}{2I_y}z^2 - \nu \cdot \frac{M_y}{2I_y}(y^2 - x^2)\right] \cdot \frac{1}{E}, \\ v &= \nu \cdot \frac{M_y}{I_y}xy \cdot \frac{1}{E}, w = -\frac{M_y}{I_y}xz \cdot \frac{1}{E}, \end{aligned} \tag{34}$$

where $I_y = bh^3/12$ is the moment of inertia about the y axis. Here the reference analytical solution in Eq. (34) is organized as the same expression as Eq. (27).

We take the element size $l_{\text{el}} = 1/16$ as example. Eq. (34) actually gives an analytical solution for $\tilde{\boldsymbol{b}}_0$ and $\tilde{\boldsymbol{b}}_1$ that

$$\begin{aligned} \tilde{b}_{I,0} &= \begin{cases} \frac{M_y}{2I_y}z^2 & \text{for degree of freedom } u, \\ 0 & \text{for degree of freedom } v, \tilde{b}_{I,1} \\ -\frac{M_y}{I_y}xz & \text{for degree of freedom } w \end{cases} \\ &= \begin{cases} -\frac{M_y}{2I_y}(y^2 - x^2) & \text{for degree of freedom } u, \\ \frac{M_y}{I_y}xy & \text{for degree of freedom } v, \\ 0 & \text{for degree of freedom } w, \end{cases} \end{aligned} \tag{35}$$

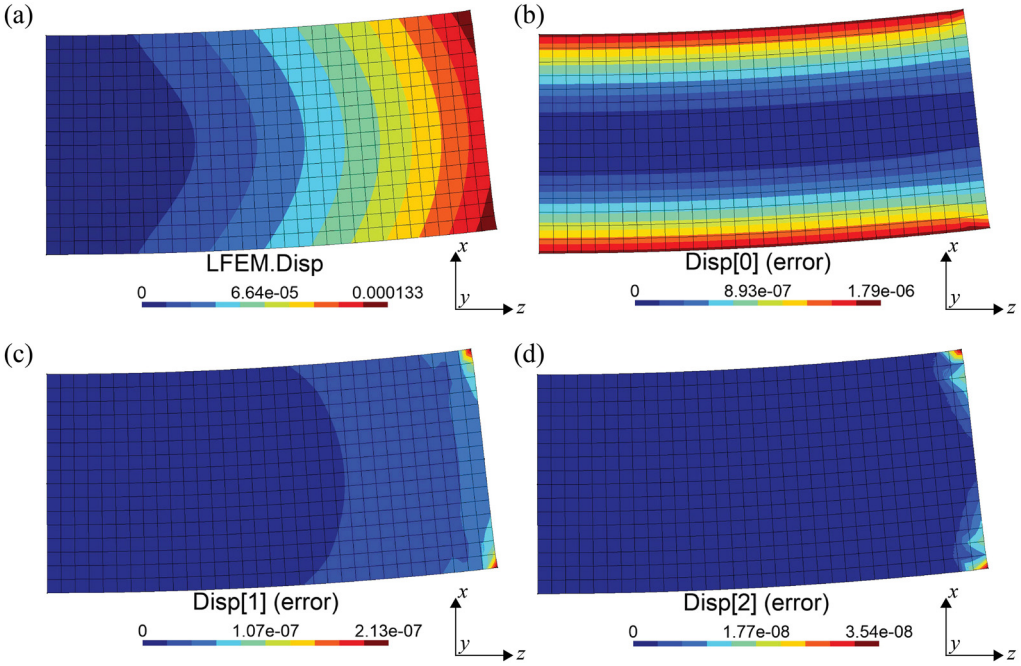

Fig. 4. Visualization of the displacement field for the pure-bending test with mesh size $l_{\text{el}} = 1/8$: (a) LFEM results as the reference solution $\boldsymbol{d}_{\text{LFEM}}$; (b) error as $\boldsymbol{d}_0 - \boldsymbol{d}_{\text{LFEM}}$; (b) error as $\boldsymbol{d}_1 - \boldsymbol{d}_{\text{LFEM}}$; (d) error as $\boldsymbol{d}_2 - \boldsymbol{d}_{\text{LFEM}}$.

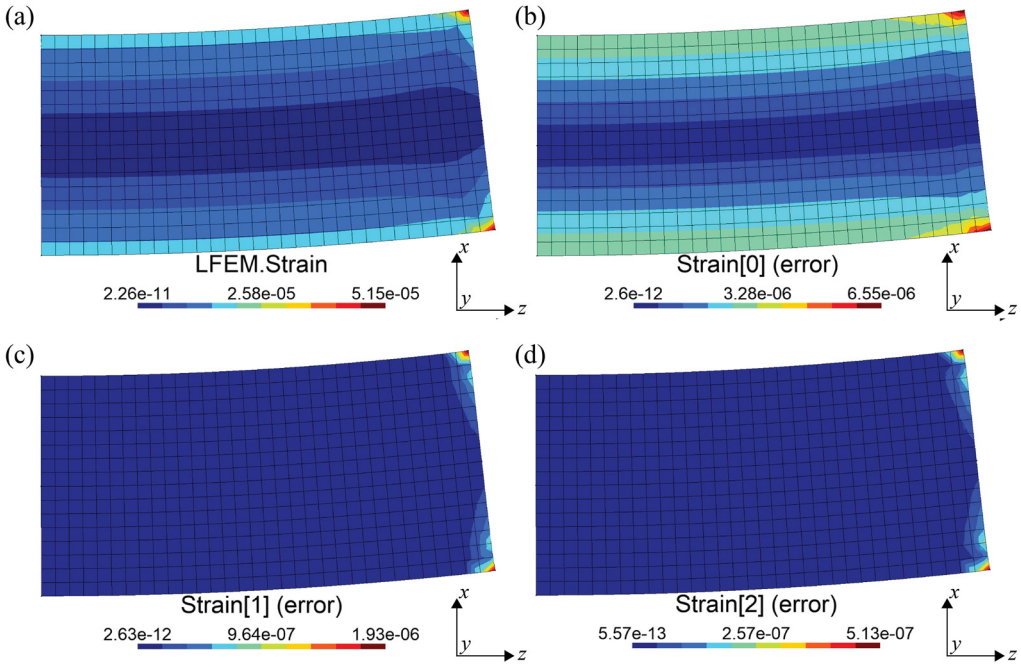

Fig. 5. Visualization of the strain field for the pure-bending test with mesh size $l_{\text{el}} = 1/8$: (a) LFEM results as the reference solution $\boldsymbol{\varepsilon}_{\text{LFEM}}$; (b) error as $\boldsymbol{\varepsilon}_0 - \boldsymbol{\varepsilon}_{\text{LFEM}}$; (b) error as $\boldsymbol{\varepsilon}_1 - \boldsymbol{\varepsilon}_{\text{LFEM}}$; (d) error as $\boldsymbol{\varepsilon}_2 - \boldsymbol{\varepsilon}_{\text{LFEM}}$.

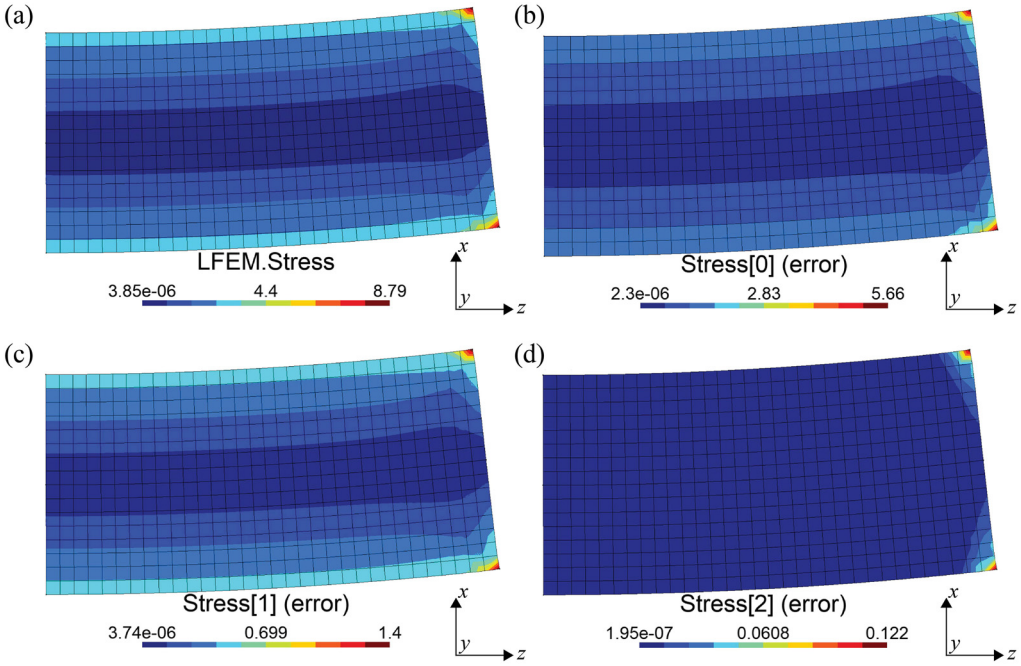

Fig. 6. Visualization of the stress field for the pure-bending test with mesh size $l_{\text{el}} = 1/8$: (a) LFEM results as reference solution $\boldsymbol{\sigma}_{\text{LFEM}}$; (b) error as $\boldsymbol{\sigma}_0 - \boldsymbol{\sigma}_{\text{LFEM}}$; (b) error as $\boldsymbol{\sigma}_1 - \boldsymbol{\sigma}_{\text{LFEM}}$; (d) error as $\boldsymbol{\sigma}_2 - \boldsymbol{\sigma}_{\text{LFEM}}$.

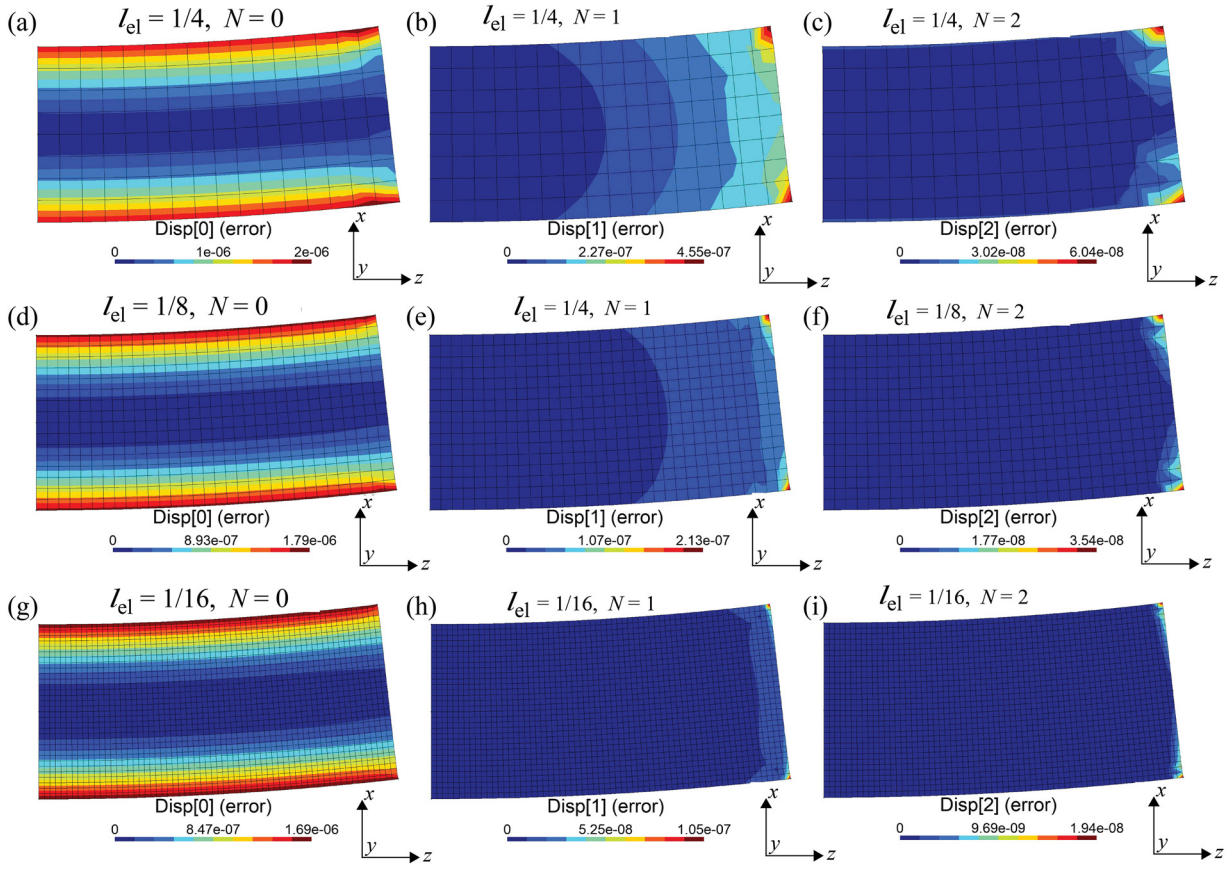

Fig. 7. Visualization of the error of the displacement field against the LFEM reference results for the pure-bending test with various mesh sizes and numbers of truncated terms: (a) $l_{el} = 1/4, N = 0$; (b) $l_{el} = 1/4, N = 1$; (c) $l_{el} = 1/4, N = 2$; (d) $l_{el} = 1/8, N = 0$; (e) $l_{el} = 1/8, N = 1$; (f) $l_{el} = 1/8, N = 2$; (g) $l_{el} = 1/16, N = 0$; (h) $l_{el} = 1/16, N = 1$; (i) $l_{el} = 1/16, N = 2$; .

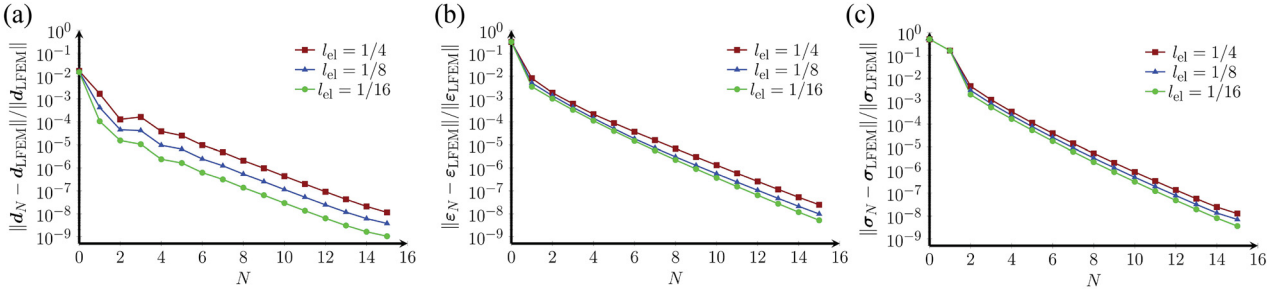

Fig. 8. Relative error under different element sizes with respect to the LFEM results: (a) displacements as $\|\boldsymbol{d}_N - \boldsymbol{d}_{\mathrm{LFEM}}\|/\|\boldsymbol{d}_{\mathrm{LFEM}}\|$; (b) strains as $\|\boldsymbol{\varepsilon}_N - \boldsymbol{\varepsilon}_{\mathrm{LFEM}}\|/\|\boldsymbol{\varepsilon}_{\mathrm{LFEM}}\|$; (c) stresses as $\|\boldsymbol{\sigma}_N - \boldsymbol{\sigma}_{\mathrm{LFEM}}\|/\|\boldsymbol{\sigma}_{\mathrm{LFEM}}\|$.

The comparisons of the four coefficient vectors $\boldsymbol{b}_{I,0}$ for u, $\boldsymbol{b}_{I,1}$ for u, $\boldsymbol{b}_{I,1}$ for v, and $\boldsymbol{b}_{I,0}$ for w are depicted in Fig. 9(a)–(d), respectively. In addition, all the other coefficient vectors are close to $\mathbf{0}$, which also matches the analytical solution.

4. Applications

4.1. Approximate analytical solution with geometric parameters

In CMAS-FE, geometric parameters such as the length of the structure cannot be considered directly, i.e., these parameters will not appear in the approximate analytical solution.

Next, we consider the cantilever-beam-bending test depicted in Fig. 10. In this example, we aim to fit an approximate analytical solution for bending stiffness with respect to geometric parameters L, h, and b. These geometric parameters may not directly appear in the truncated solution $\boldsymbol{d}_N$. However, we will repeat various tests with different L and h values, while the width b can be set as 1 all the time. For a beam structure, we assume $h/L < 0.6$.

We define the deflection stiffness K as

$$K = \frac{F}{\delta} = b\frac{E}{(1-\nu)(1+2\nu)}\left(c_0 + c_1\nu + c_2\nu^2\right), \tag{36}$$

where F is the total reaction force at the right edge of the beam. Dimensionless coefficients c_k, $k = 0, 1, 2$ depends on the geometric parameters h and L. We use the CMAS-FE for all the pairs of (L, h) such that $L = 5, 6, \ldots, 20$ and $h = 2, 3, \ldots, 6$, and obtain F in series form. Next, we use base function $(h/L)^3$ and $(h/L)^4$ to approximate the coefficients c_k,

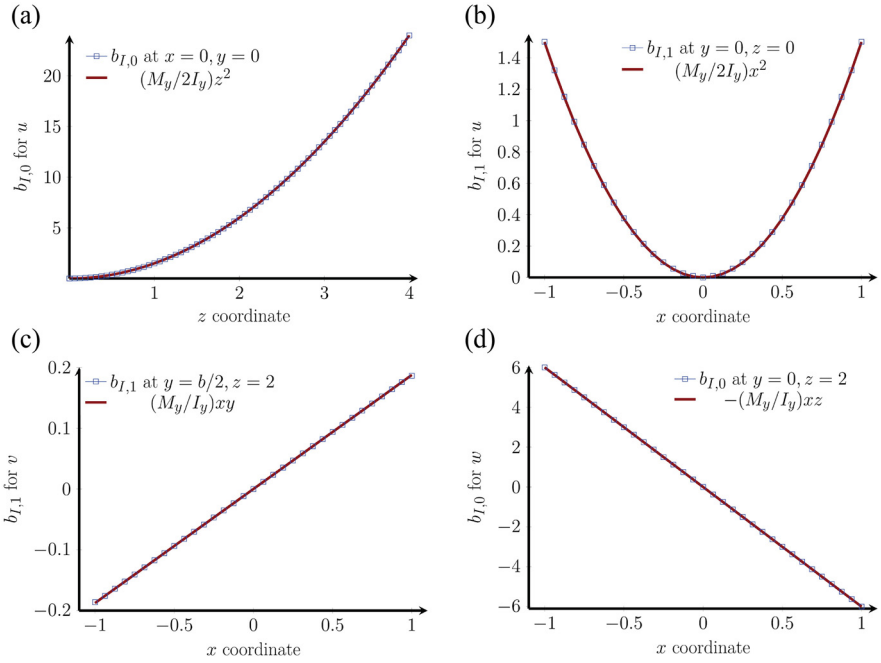

Fig. 9. Verification of the coefficient vector $\tilde{b}_{I,k}$ with analytical solution: (a) verify $\tilde{b}_{I,0}$ for u; (b) verify $\tilde{b}_{I,1}$ for u; (b) verify $\tilde{b}_{I,1}$ for v; (b) verify $\tilde{b}_{I,0}$ for w.

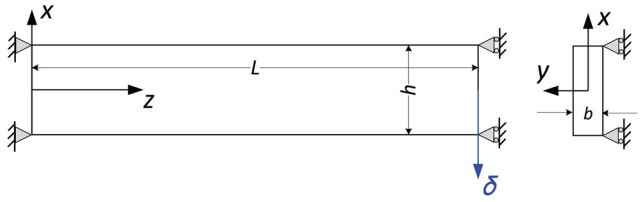

Fig. 10. Sketch of cantilever-beam-bending test with zero-angle and unit-deflection at the end.

$k = 0, 1, 2$ and obtain

$$\begin{bmatrix} c_0 \\ c_1 \\ c_2 \end{bmatrix} = \begin{bmatrix} 1.09273 & -0.921761 \\ -1.17948 & 0.673446 \\ -2.01790 & 2.24214 \end{bmatrix} \begin{bmatrix} (h/L)^3 \\ (h/L)^4 \end{bmatrix}, \tag{37}$$

or

$$K = \frac{Eb}{(1-\nu)(1+2\nu)} \left[\left(1.09273 - 1.17948\nu - 2.01790\nu^2\right)\left(\frac{h}{L}\right)^3 - \left(0.921761 - 0.673446\nu - 2.24214\nu^2\right)\left(\frac{h}{L}\right)^4 \right]. \tag{38}$$

Here the base function $(h/L)^p$ for arbitrary $p \in \mathbb{N}$ can be used to enrich the interpolation function. However, the numerical optimization process shows that the terms $(h/L)^3$ and $(h/L)^4$ are dominant. From Fig. 11, we may see that the interpolated coefficients in Eq. (37) are quite accurate compared with the results given by the CMAS-FE.

4.2. Stress intensity factor for a straight crack embedded in a square plate

Next, we consider deriving an approximate analytical expression of stress intensity factor (SIF) for the problem depicted in Fig. 12, where a crack with length $2w$ is embedded in a square plate under remote stress in the y direction. From linear elastic fracture mechanics we know that the SIF

$$K_I = \sqrt{\pi w}\sigma_y, \tag{39}$$

when $A \to \infty$. Here we use the CMAS-FE to derive the SIF with finite square size A. Finite element meshes with some selected square sizes are depicted in Fig. 13. We can obtain SIFs with A as listed in Table 1. Here the CMAS-FE can determine the values for $\tilde{k}_0$ and $\tilde{k}_1$ defined as

$$K_I(A) \approx \sqrt{\pi w}\sigma_y\left[\tilde{k}_0 + \tilde{k}_1\nu\right]. \tag{40}$$

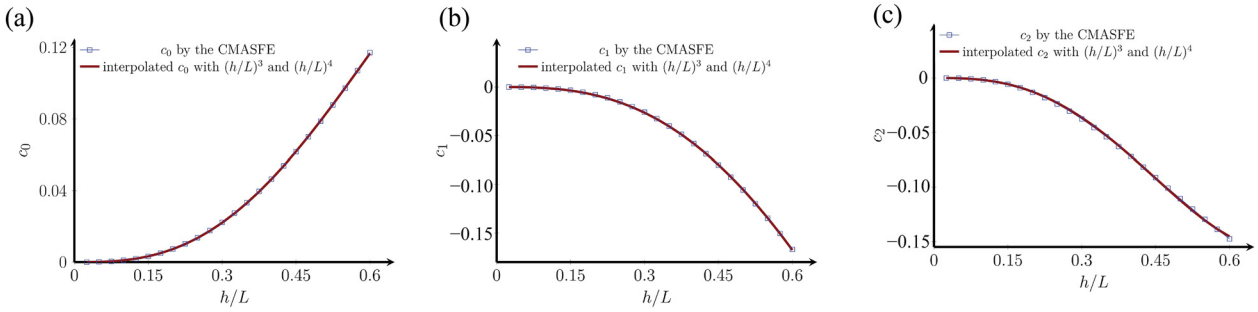

Fig. 11. Comparison of the coefficient between the CMAS-FE and the interpolated value: (a) coefficient c_0; (b) coefficient c_1; (c) coefficient c_2.

Table 1
Data for $K_I(A) \approx \sqrt{\pi w}\sigma_y[\tilde{k}_0 + \tilde{k}_1 \nu]$ and $K_I(A) \approx \sqrt{\pi w}\sigma_y[\hat{k}_0 + \hat{k}_1 \nu]$ with various square sizes.

A	$\tilde{k}_0$	$\tilde{k}_1$	$\hat{k}_0$	$\hat{k}_1$	A	$\tilde{k}_0$	$\tilde{k}_1$	$\hat{k}_0$	$\hat{k}_1$
3	1.789100	0.019000	1.783678	0.019644	8	1.106200	0.022200	1.101595	0.023309
4	1.422200	0.016900	1.433256	0.015413	9	1.082900	0.024300	1.079112	0.025242
5	1.268800	0.017300	1.272660	0.016520	10	1.065200	0.026600	1.063195	0.026940
6	1.187800	0.018500	1.186286	0.018778	11	1.051000	0.029000	1.051540	0.028430
7	1.138800	0.020200	1.134724	0.021135	12	1.039300	0.031500	1.042767	0.029740
∞	1	0	1.0027	0.0483					

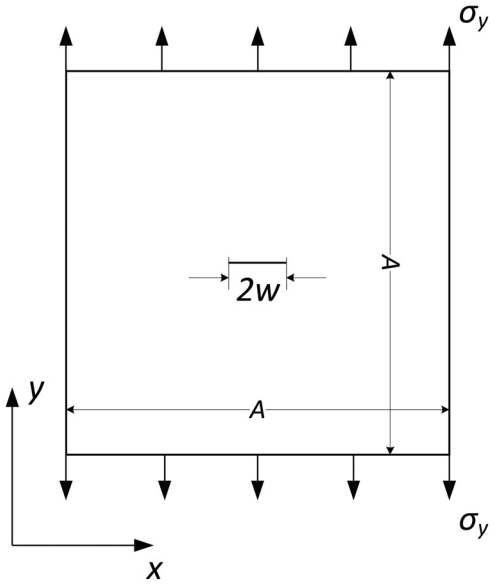

Fig. 12. Sketch of a straight crack embedded in a square plate under remote stress in y direction.

Through the collected data with various square sizes, we can obtain the following approximated SIF with dependence on A such that:

$$K_I = \sqrt{\pi w}\sigma_y \left[\underbrace{1.0027 - 0.1399\frac{w}{A} + 7.4485\frac{w^2}{A^2}}_{\equiv \tilde{k}_0} + \nu \left(\underbrace{0.0483 - 0.2683\frac{w}{A} + 0.547\frac{w^2}{A^2}}_{\equiv \tilde{k}_1} \right) \right], \tag{41}$$

where the values of $\hat{k}_0$ and $\hat{k}_1$ are also listed in Table 1 for comparison with $\tilde{k}_0$ and $\tilde{k}_1$, respectively.

Since the problem considers an embedded crack, the values of strain and stress may diverge near the crack tip. Here, we check the relative errors of the displacement, strain, and stress with various w/A ratios, as depicted in Fig. 14. The comparison shows that the approximate CAMS-FE results can converge to the classic LFEM results when the number of terms is sufficiently large.

4.3. Bending stiffness for a square plate with an ellipse hole

Consider the square plate with an ellipse hole depicted in Fig. 15. The length along the x and y directions is $L = 1$, and the thickness is $h = 0.2$. The semi-major and semi-minor axes of the ellipse are $a = 0.3$ and $b = 0.1$, respectively. A rotation angle θ is introduced, as depicted in Fig. 15. We use the CMAS-FE to derive an approximated bending stiffness as a function of θ only.

To collect sufficient data, seven CMAS-FE simulations are tested with $\theta = \{0, \pi/12, \pi/6, \ldots, \pi/2\}$. Four selected hexahedron finite element meshes are depicted in Fig. 16. Here we only study the bending stiffness as function of θ, and the interpolation yields:

$$\begin{aligned} K = \frac{1}{1000}\frac{E}{(1-\nu)(1+2\nu)} \Big\{ & \left[1.771380 - 0.2481020\sin^2\theta - 0.111461\sin^4\theta\right] \\ & - \left[1.843250 - 0.0446600\sin^2\theta - 0.251424\sin^4\theta\right]\nu \\ & - \left[2.599070 - 0.7011710\sin^2\theta + 0.133704\sin^4\theta\right]\nu^2 \\ & - \left[0.810572 - 0.0698223\sin^2\theta - 0.177138\sin^4\theta\right]\nu^3 \Big\}. \end{aligned} \tag{42}$$

In addition, we demonstrate the stress error distributions for various values of θ, as depicted in Fig. 17 with $E = 2.1 \times 10^5$ MPa and $\nu = 0.23$. We can see that the maximum error occurs at the edges, where stress concentration or a high stress gradient occurs.

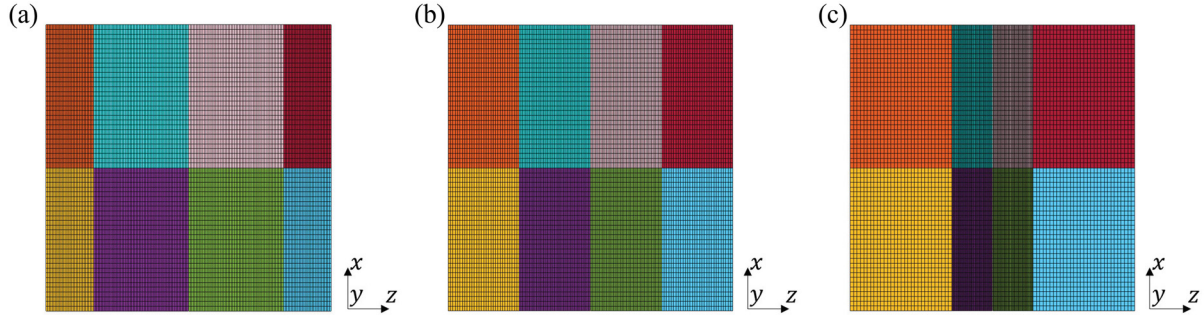

Fig. 13. Selected structured quadrilateral mesh for straight cracks embedded in a square plate with $w = 2$: (a) $A = 3$, (b) $A = 4$, and (c) $A = 7$.

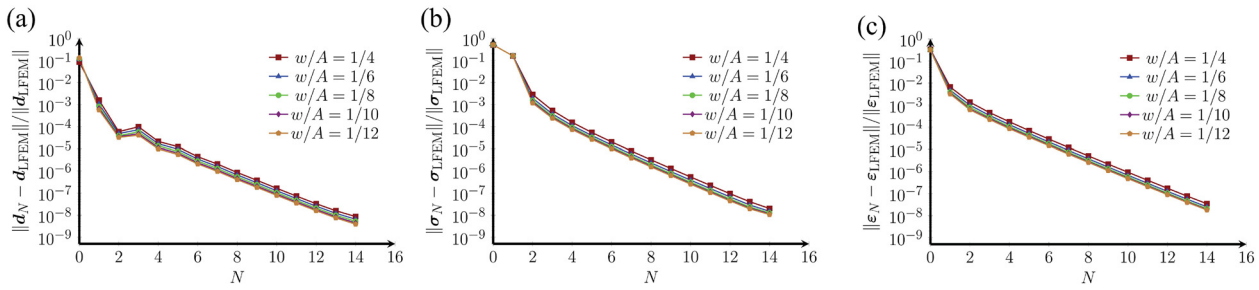

Fig. 14. Relative error under different w/A ratios with respect to the LFEM results: (a) displacements as $\|\boldsymbol{d}_N - \boldsymbol{d}_{\mathrm{LFEM}}\|/\|\boldsymbol{d}_{\mathrm{LFEM}}\|$; (b) strains as $\|\boldsymbol{\varepsilon}_N - \boldsymbol{\varepsilon}_{\mathrm{LFEM}}\|/\|\boldsymbol{\varepsilon}_{\mathrm{LFEM}}\|$; (c) stresses as $\|\boldsymbol{\sigma}_N - \boldsymbol{\sigma}_{\mathrm{LFEM}}\|/\|\boldsymbol{\sigma}_{\mathrm{LFEM}}\|$.

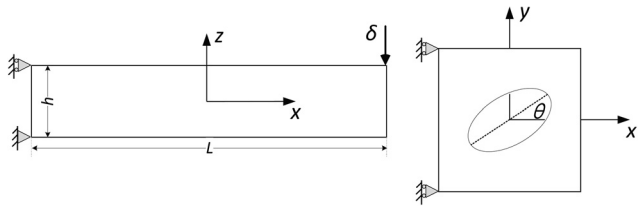

Fig. 15. Sketch of a square plate with ellipse hole.

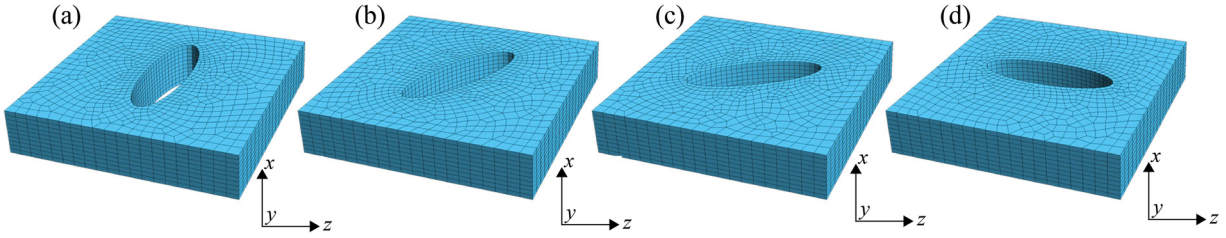

Fig. 16. Selected hexahedron mesh for square plate ($L = 1$, $h = 0.2$, $a = 0.3$, $b = 0.1$) with an ellipse hole: (a) $\theta = 0$, (b) $\theta = \pi/6$, (c) $\theta = \pi/3$, and (d) $\theta = \pi/2$.

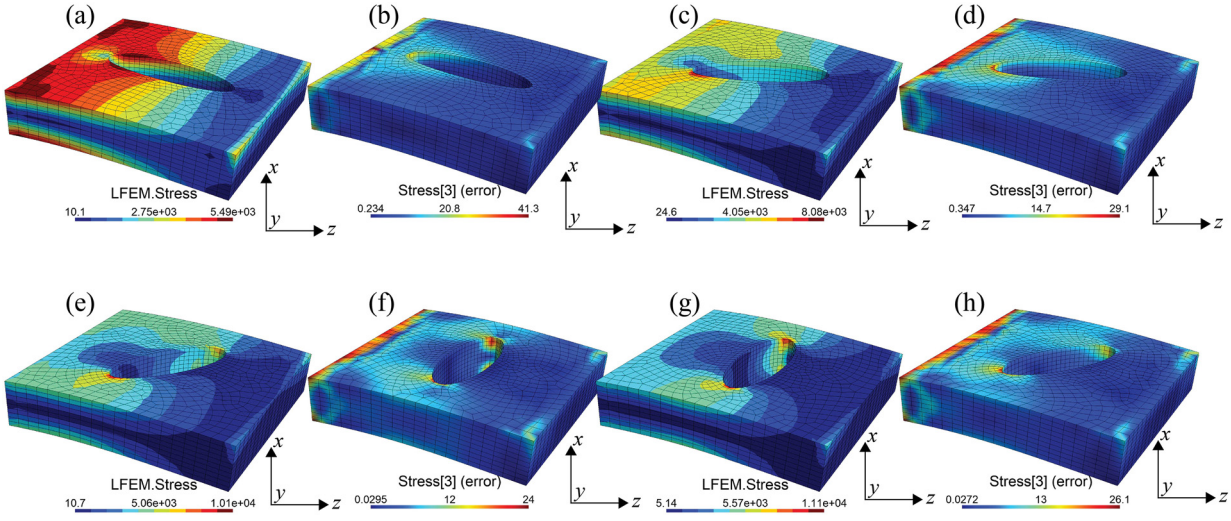

Fig. 17. Visualization of the stress field for plate-with-ellipse-hole bending test: (a) LFEM results as reference solution $\boldsymbol{\sigma}_{\mathrm{LFEM}}$ with $\theta = 0$; (b) error as $\boldsymbol{\sigma}_3 - \boldsymbol{\sigma}_{\mathrm{LFEM}}$ with $\theta = 0$; (c) LFEM results as reference solution $\boldsymbol{\sigma}_{\mathrm{LFEM}}$ with $\theta = \pi/6$; (d) error as $\boldsymbol{\sigma}_3 - \boldsymbol{\sigma}_{\mathrm{LFEM}}$ with $\theta = \pi/6$; (e) LFEM results as reference solution $\boldsymbol{\sigma}_{\mathrm{LFEM}}$ with $\theta = \pi/3$; (f) error as $\boldsymbol{\sigma}_3 - \boldsymbol{\sigma}_{\mathrm{LFEM}}$ with $\theta = \pi/3$; (g) LFEM results as reference solution $\boldsymbol{\sigma}_{\mathrm{LFEM}}$ with $\theta = \pi/2$; (h) error as $\boldsymbol{\sigma}_3 - \boldsymbol{\sigma}_{\mathrm{LFEM}}$ with $\theta = \pi/2$;.

5. Conclusion

This study introduces a novel methodology that aims to obtain an approximate analytical solution for an isotropic homogeneous elastic medium with displacement and traction boundary conditions. The analytical solution is derived by solving a specific numerical problem defined by linear finite element method (LFEM), and the method is named the computational method for analytical solution with finite element (CMAS-FE). In CMAS-FE, we treat Young's modulus E and Poisson's ratio ν as two symbols in the global system of linear equations in the LFEM.

One can then obtain the displacement at nodes as an infinite series in terms of the Poisson's ratio. Accordingly, CMAS-FE can yield displacement and reaction forces at nodes, strain and stress at quadrature points without physical values of E or ν. In this work, the CMAS-FE is verified by a patch test and pure-bending test. We study the convergence by mesh refinement and increasing number of truncated terms.

One limitation of the CMAS-FE is that geometric parameters cannot be directly considered in the approximate analytical solution. We must first define a domain with a well-defined geometric parameters and mesh it into finite elements, and then obtain one approximate analytical solution through the CMAS-FE with only E and ν. However, we can repeat this process with various combination of the geometric parameters, and obtain an approximate solution with geometric parameters with interpolation or even the deep neural network method. In this work, the CMAS-FE is applied to obtain an approximate bending stiffness of a beam structure without requiring beam slenderness. In addition, the CMAS-FE is also used to estimate an approximate stress intensity factor for a straight crack within a square-shaped plate.

The restriction of the problem is another limitation of the CMAS-FE. Either geometric or material nonlinear problem requires NEWTON-RAPHSON iterative process, where the global stiffness matrix depends on the displacement field as well as the intrinsic state variables. In this way, we cannot take inverse in a symbolic sense. However, extending the CMAS-FE to a linear heterogeneous problem could be a focus of future work.

Declaration of competing interest

The authors declare that they have no known competing financial interests or personal relationships that could have appeared to influence the work reported in this paper.

CRediT authorship contribution statement

Jiajia Yue: Visualization, Formal analysis. **Zifeng Yuan:** Writing – original draft, Methodology.

Acknowledgment

This work was supported by the National Natural Science Foundation of China Excellence Research Group Program for "Multiscale Problems in Nonlinear Mechanics" (Grant No. 12588201), the National Key R & D Program of China (Grant No. 2023YFA1008901), and the National Natural Science Foundation of China (Grant No. 12172009). The research is also supported by "The Fundamental Research Funds for the Central Universities, Peking University".

References

[1] C.F. Lü, C.W. Lim, W.Q. Chen, Semi-analytical analysis for multi-directional functionally graded plates: 3-d elasticity solutions, Int. J. Numer. Methods Eng. 79 (1) (2009) 25–44, doi:10.1002/nme.2555.
[2] J. Korelc, Semi-analytical solution of path-independent nonlinear finite element models, Finite Elem. Anal. Des. 47 (3) (2011) 281–287, doi:10.1016/j.finel.2010.10.006.
[3] Y.F. Zhao, X.C. Shang, E. Pan, Analytical solutions of uniform extended dislocations and tractions over a circular area in anisotropic magnetoelectroelastic bimaterials, Acta Mech. Sin. 29 (1) (2013) 73–84, doi:10.1007/s10409-013-0056-8.
[4] A. Pouya, Ellipsoidal anisotropy in linear elasticity: approximation models and analytical solutions, Int. J. Solids Struct. 48 (14–15) (2011) 2245–2254, doi:10.1016/j.ijsolstr.2011.03.028.
[5] Z.F.F. Yuan, H.M.M. Yin, Elastic green's functions for a specific graded material with a quadratic variation of elasticity, J. Appl. Mech.-Trans. Asme 78 (2) (2011), doi:10.1115/1.4002615.
[6] P. Franciosi, S. Barboura, Y. Charles, Analytical mean green operators/eshelby tensors for patterns of coaxial finite long or flat cylinders in isotropic matrices, Int. J. Solids Struct. 66 (2015) 1–19, doi:10.1016/j.ijsolstr.2015.03.027.
[7] P. Franciosi, A generic green operator based analytical solution form for all the effective generalized elastic-like moduli of n-phase laminates, Int. J. Solids Struct. 232 (2021), doi:10.1016/j.ijsolstr.2021.111072.
[8] S.M. Shang, J.X. Xiao, T.L. Jiang, W.H. Zhang, Analytical solution of multilayered structures with green's function, Int. J. Solids Struct. 290 (2024), doi:10.1016/j.ijsolstr.2023.112636.
[9] C. Oskay, J. Fish, Eigendeformation-based reduced order homogenization for failure analysis of heterogeneous materials, Comput. Methods Appl. Mech. Eng. 196 (7) (2007) 1216–1243, doi:10.1016/j.cma.2006.08.015.
[10] Z. Yuan, J. Fish, Multiple scale eigendeformation-based reduced order homogenization, Comput. Methods Appl. Mech. Eng. 198 (21–26) (2009) 2016–2038, doi:10.1016/j.cma.2008.12.038.
[11] X. Zhang, C. Oskay, Eigenstrain based reduced order homogenization for polycrystalline materials, Comput. Methods Appl. Mech. Eng. 297 (2015) 408–436, doi:10.1016/j.cma.2015.09.006.
[12] S.Q. Huang, J.J. Yue, X.B. Liu, P. Ren, L. Zu, Z.F. Yuan, A framework of defining constitutive model for fibrous composite material through reduced-order-homogenization method with analytical influence functions, Compos. Struct. 314 (2023), doi:10.1016/j.compstruct.2023.116968.
[13] Y.S. Thube, T.P. Gotkhindi, A simple, robust novel williams series-based FE-analytical hybrid technique for evaluation of SIFs and higher order coefficients, Theor. Appl. Fract. Mech. 127 (2023), doi:10.1016/j.tafmec.2023.104101.
[14] Y.X. Sun, Z.H. Xiang, A semi-analytical quasi-brittle fracture criterion for elliptical notches, Eng. Fract. Mech. 266 (2022), doi:10.1016/j.engfracmech.2022.108405.
[15] S.Z. Xing, X.J. Pei, J.F. Mei, C.B. Zhen, S.J. Su, An analytical approach for evaluation of linear elastic stress fields around sharp v-shaped notches in plates, Eng. Fract. Mech. 292 (2023), doi:10.1016/j.engfracmech.2023.109584.
[16] F. Pistorio, D. Clerici, A. Somá, Analytical computation of stress intensity factor for active material particles of lithium ion batteries, Eng. Fract. Mech. 292 (2023), doi:10.1016/j.engfracmech.2023.109597.
[17] Y.M. Li, M.P. Hoang, B. Abbes, F. Abbes, Y.Q. Guo, Analytical homogenization for stretch and bending of honeycomb sandwich plates with skin and height effects, Compos. Struct. 120 (2015) 406–416, doi:10.1016/j.compstruct.2014.10.028.
[18] Y.M. Li, F. Abbes, M.P. Hoang, B. Abbes, Y.Q. Guo, Analytical homogenization for in-plane shear, torsion and transverse shear of honeycomb core with skin and thickness effects, Compos. Struct. 140 (2016) 453–462, doi:10.1016/j.compstruct.2016.01.007.
[19] G. Bartolozzi, N. Baldanzini, M. Pierini, G. Zonfrillo, Static and dynamic experimental validation of analytical homogenization models for corrugated core sandwich panels, Compos. Struct. 125 (2015) 343–353, doi:10.1016/j.compstruct.2015.02.014.
[20] J. Kalisch, R. Glüge, Analytical homogenization of linear elasticity based on the interface orientation distribution - a complement to the self-consistent approach, Compos. Struct. 126 (2015) 398–416, doi:10.1016/j.compstruct.2015.02.072.
[21] M. Shakiba, D.R. Brandyberry, S. Zacek, P.H. Geubelle, Transverse failure of carbon fiber composites: analytical sensitivity to the distribution of fiber/matrix interface properties, Int. J. Numer. Methods Eng. 120 (5) (2019) 650–665, doi:10.1002/nme.6151.
[22] S. Heide-Jorgensen, C.H. Ibsen, M.K. Budzik, Effective through-the-thickness diffusivity of plain-woven composite from analytical homogenization, Compos. Sci. Technol. 202 (2021), doi:10.1016/j.compscitech.2020.108552.
[23] L. Huang, X. Liu, X. Liu, X.Y. Zhao, Analytical homogenization for equivalent in-plane elastic moduli of multi-material honeycombs, Compos. Struct. 325 (2023), doi:10.1016/j.compstruct.2023.117586.
[24] Z. Guo, X. Liu, L. Huang, S. Adhikari, X.F. Liang, Analytical homogenization for equivalent in-plane elastic moduli of prestressed lattices based on the micropolar elasticity model, Compos. Struct. 346 (2024), doi:10.1016/j.compstruct.2024.118391.
[25] S. Huang, Z. Yuan, Strain concentration factor of heterogeneous materials and analytical influence functions based on eshelby tensor, Theor. Appl. Mech. Lett. 14 (4) (2024) 100542, doi:10.1016/j.taml.2024.100542.
[26] A. Salvadori, Analytical integrations in 2d BEM elasticity, Int. J. Numer. Methods Eng. 53 (7) (2002) 1695–1719, doi:10.1002/nme.359.
[27] Y.C. Shiah, Analytical transformation of the volume integral in the boundary integral equation for 3d anisotropic elastostatics involving body force, Comput. Methods Appl. Mech. Eng. 278 (2014) 404–422, doi:10.1016/j.cma.2014.05.013.
[28] F. Krome, H. Gravenkamp, A semi-analytical curved element for linear elasticity based on the scaled boundary finite element method, Int. J. Numer. Methods Eng. 109 (6) (2017) 790–808, doi:10.1002/nme.5306.
[29] F. Marmo, L. Rosati, Analytical integration of elasto-plastic uniaxial constitutive laws over arbitrary sections, Int. J. Numer. Methods Eng. 91 (9) (2012) 990–1022, doi:10.1002/nme.4316.
[30] R. Hospital-Bravo, J. Sarrate, P. Díez, A semi-analytical scheme for highly oscillatory integrals over tetrahedra, Int. J. Numer. Methods Eng. 111 (8) (2017) 703–723, doi:10.1002/nme.5474.
[31] B. Miled, I. Doghri, L. Delannay, Coupled viscoelastic-viscoplastic modeling of homogeneous and isotropic polymers: numerical algorithm and analytical solutions, Comput. Methods Appl. Mech. Eng. 200 (47–48) (2011) 3381–3394, doi:10.1016/j.cma.2011.08.015.
[32] M. Cervera, J.Y. Wu, M. Chiumenti, S. Kim, Strain localization analysis of hill's orthotropic elastoplasticity: analytical results and numerical verification, Comput. Mech. 65 (2) (2020) 533–554, doi:10.1007/s00466-019-01782-4.